

# Interlayer Magnetic Coupling in FePS<sub>3</sub> and NiPS<sub>3</sub> Stacked Bilayers

Andrea León,<sup>1,4,\*</sup> Beatriz Costa,<sup>2,3,\*</sup> Thomas Heine,<sup>2,3,4,5</sup> Thomas Brumme<sup>4</sup>

<sup>1</sup>Departamento de Física, Facultad de Ciencias, Universidad de Chile, Casilla 653, Santiago, Chile.

<sup>2</sup>Helmholtz-Zentrum Dresden-Rossendorf, Bautzner Landstr. 400, 01328 Dresden, Germany.

<sup>3</sup>Center for Advanced Systems Understanding, CASUS, Untermarkt 20, 02826 Görlitz, Germany.

<sup>4</sup>Chair of Theoretical Chemistry, Technische Universität Dresden, Bergstrasse 66, 01069 Dresden, Germany.

<sup>5</sup>Yonsei University and ibs-cnm, Seodaemun-gu, Seoul 120-749, Republic of Korea.

\*These authors contributed equally to this work.

18th October 2024

## Abstract

Single layers of transition-metal thiophosphates (2D-TMPS<sub>3</sub>) van der Waals magnets are an ideal platform for studying antiferromagnetic interactions in two dimensions. However, the magnetic coupling mechanism between two or more individual layers of these materials remains mostly unexplored. This study presents a density-functional based analysis and analytical models to describe the magnetic configurations of FePS<sub>3</sub> and NiPS<sub>3</sub> stacked bilayers. We explore the interplay between magnetic configurations and stacking shift, therefore identifying the mechanisms that result in either ferromagnetic or antiferromagnetic coupling between layers. Our findings indicate that the stacking with the lowest energy is metal-dependent, and the interlayer magnetic configuration (ferromagnetic or antiferromagnetic) varies based on the stacking type and the metal involved. Using an Ising-Hamiltonian model and a tight-binding model based on Wannier functions, we show that interlayer exchange interactions must be considered up to the third nearest neighbor and to elucidate the superexchange mechanism for the NiPS<sub>3</sub> system.

## 1 Introduction

Stacking engineering in van der Waals (vdW) layered magnetic systems offers new ways to manipulate and study magnetic phases [1]. Techniques such as layer shifting, rotation, moiré patterns, and forming heterostructures by stacking different layers are currently employed in this field [2]. Particularly, the exploration of stacked antiferromagnetic (AFM) and semiconducting materials is revealing new physical phenomena with potentially transformative impacts [3, 4]. The 2D-TMPS<sub>3</sub> (TM = transition metal atom) systems being semiconductors and antiferromagnets are garnering attention for their unique optical properties coupled with their magnetic ordering. Currently, utilizing stacking degrees of freedom to merge these properties opens new avenues for investigating magnetic phenomena and interface effects [5, 6]. In this context, research focused on unraveling the role of AFM order, stacking degrees of freedom, and the role of the TM atoms is necessary for further understanding and controlling desired properties in the search for functional materials.

The first-row TMPS<sub>3</sub> (TM = Mn, Fe, Ni, and Co) family exhibits diverse AFM properties [7]. They can behave like Heisenberg (MnPS<sub>3</sub> [8]), Ising (FePS<sub>3</sub> [9]), and XY-type (CoPS<sub>3</sub> [10] and NiPS<sub>3</sub> [4]) antiferromagnets. Besides their magnetic properties, these materials

show intriguing optical properties that vary from bulk to layered structures, including optical excitations ranging from near IR to UV [11] and excitons with large binding energies [12, 13]. They can be exfoliated into a few atomic layers, enabling studies on magnetic ordering and dimensionality [14, 15]. However, detailed measurements are challenging due to the complexity of experimental setups for materials with zero total magnetization [16]. These materials' magnetic, electronic, and optical properties offer an exciting landscape for optoelectronic and spintronic applications [5, 17, 18].

TMPS<sub>3</sub> monolayers exhibit magnetic properties dictated by superexchange interactions between metal nearest neighbors (NN)[19, 20]. While intralayer interactions are well-studied, interlayer interactions remain relatively unexplored [21]. In other bilayer systems, e.g, the CrX<sub>3</sub> family [22, 23], the magnetic interlayer interactions are influenced by the contributions of first, second, or even third neighbors, requiring mechanisms beyond superexchange to be understood. Unlike FM layers, the stacked AFM sheets cannot be simply defined with FM or AFM coupling (denoted as FMc and AFMc, see Fig. 1). Depending on the in-plane magnetic configuration (Néel, zigzag, or stripy), the NN interactions between layers can be AFMc or FMc, which could lead to magnetic competition or spin frustration. This frustration depends on the number of metal NN, distances, and the superexchange mechanism involved among the metal and sulfide atoms of the

<sup>1</sup>andrea.leon@uchile.cl

<sup>2</sup>thomas.brumme@tu-dresden.de

bottom and top layers. Models that consider distance and hopping processes are necessary to understand the mechanism behind of the magnetic interactions in AFM bilayers.

While interlayer interactions in TMPS<sub>3</sub> systems are generally weaker than intralayer interactions, significant interlayer effects vary with the TM type [24]. For example, strong interlayer interactions in NiPS<sub>3</sub> are evident in processes like layer exfoliation and under pressure [25]. Conversely, Raman studies suggest weaker interlayer couplings in FePS<sub>3</sub> and MnPS<sub>3</sub>, with FePS<sub>3</sub> showing stronger effects than MnPS<sub>3</sub> [26]. However, systematic theoretical studies on the influence of layering are lacking, which are crucial for manipulating AFM magnetic phases.

In this work, we study the influence of stacking on the magnetic coupling between layers and the electronic properties in bilayer FePS<sub>3</sub> and NiPS<sub>3</sub>. First, we investigate the total energy of the bilayer systems to establish the magnetic ground state. Second, we computed the exchange constant using the classical Ising model. For a second method based on Green's functions, we constructed Wannier functions from first principles. Then, we applied a spin rotation to Green's functions, providing a tight-binding (TB) Hamiltonian model to calculate the exchange constant. Our findings indicate that the most stable stacking and the magnetic coupling between layers depend on the metal atom. Through the solution of the Ising and TB Hamiltonian in the bilayers, we find that the most substantial interlayer exchange interaction occurs for the second or third NN, depending on the stacking and the metal atom. We focus on NiPS<sub>3</sub>, which exhibits stronger exchange interactions than FePS<sub>3</sub>, in agreement with experimental findings [25, 26]. With the advent of Wannier orbitals, we find that the contributions to the interlayer magnetic exchange are determined by the alignment or not of the *p* orbitals of the sulfur atoms in each layer.

## 2 Computational details

We used density functional theory (DFT) with the Perdew-Burke-Ernzerhof (PBE) generalized gradient approximation functional [27], implemented in the Vienna ab initio Simulation Package (VASP) [28], for our theoretical analysis using the plane-wave pseudopotential method. To account for London dispersion forces, we have employed the van der Waals (vdW) approximation optB86b-vdW [29]. Using this approach, we have achieved a good agreement with the lattice parameters and interlayer distances as reported in the bulk [26, 30, 31] (see, supplemental material (SM) SII). A Hubbard on-site Coulomb parameter of  $U = 5$  eV is used for the Fe and Ni atoms to accurately take into account the electronic correlations [32] along the Dudarev approach [33]. Additionally, we have performed calcu-

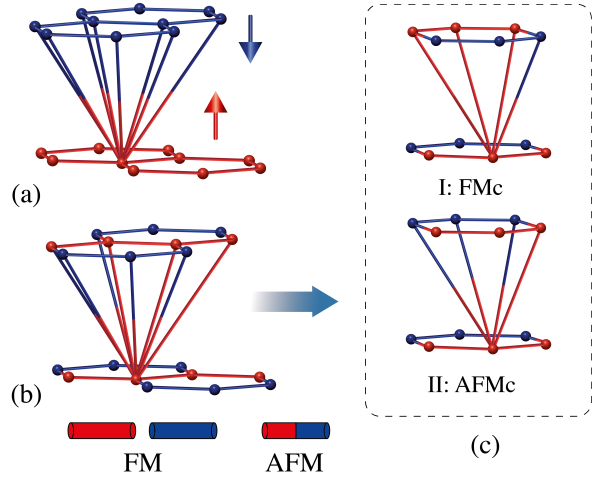


Figure 1: Illustration of two possible configurations for achieving AFM bilayers: (a) by coupling two FM layers of opposite spin, and (b) stacking two AFM layers. (c) Configuration I (I) and Configuration II (II), which denotes two possible magnetic coupling between the layers, defined as: ferromagnetic and antiferromagnetic interaction between first neighbors.

lations with  $U = 3.0, 4.0, 6.0$  eV to study the influence of the Hubbard- $U$  repulsion on specific properties. For the structural optimization of the bilayers, we include 25 Å of vacuum space to minimize the interaction between periodically repeated images along the *z*-axis. The full structural optimizations including the lattice of the bilayer systems are performed with a force convergence of  $10^{-3}$  eV/Å<sup>-1</sup> for each atom and a plane-wave energy cutoff of 500 eV. Regular Monkhorst-Pack [34] grids of  $11 \times 5 \times 1$  for the atomic relaxation, and  $15 \times 9 \times 1$  for the self-consistent calculation have been used.

The exchange parameters were calculated through the Ising model and the TB2J python package [35]. For the second method, a tight-binding model using localized Wannier functions (WF) as implemented in the Wannier90 code [36] is derived from the DFT results. More details about the Wannierization can be found in SI section.

## 3 Results

Bulk TMPS<sub>3</sub> crystallizes in a monoclinic structure with centrosymmetric  $C2/m$  point symmetry. The monolayers are then stacked in the *c* direction in an AB manner. Since two P atoms and six S atoms are covalently bonded among themselves, forming a  $(P_2S_6)^{4-}$  anion complex, each transition metal has a formal charge of +2. NiPS<sub>3</sub> and FePS<sub>3</sub> exhibit inversion symmetric zig-zag AFM order [16, 37–42]. Both systems have trigonally distorted MS<sub>6</sub> octahedra forming an edge-sharing layered honeycomb lattice in the **a/b** plane. In contrast to NiPS<sub>3</sub>, FePS<sub>3</sub> displays enhanced trigonally distorted FeS<sub>6</sub> octahedra (Fe-S bonds are not equivalent,

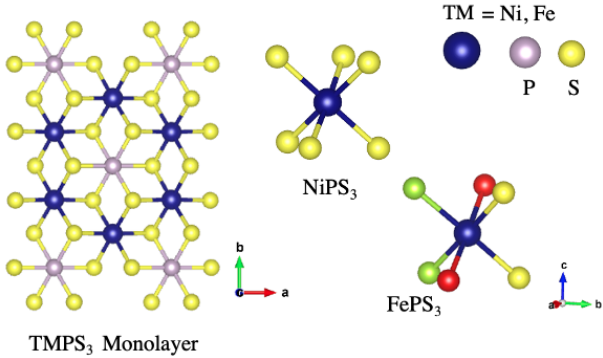


Figure 2: Monolayer structure for  $\text{TMPS}_3$ ,  $\text{TM} = \text{Fe}$  and  $\text{Ni}$ .  $\text{NiPS}_3$  exhibits a nearly perfect octahedral environment, while  $\text{FePS}_3$  displays a distorted octahedra due to the different  $\text{Fe-S}$  bonding. The  $\text{Fe-S}$  color bonds symbolize the non-equivalent length.

see Fig. 2) [43][44].

First, we analyzed several stackings of bilayer  $\text{TMPS}_3$ . These stackings were constructed starting with the fully relaxed monolayers, where the upper layer is rigidly shifted by a shift  $\delta$  (in units of the lattice constant) along  $\mathbf{a}$  ([100]) and  $\mathbf{b}$  ([010]). Fig. 3 shows the non-equivalent high-symmetry stackings corresponding to shifts in which the sulfur atoms are above the metal or around the P dumbbell. The nomenclature of the stackings is similar to the one introduced by Yu *et al.* for transition-metal dichalcogenides [45]. The different stackings are labeled  $M_b^a$ , where M stands for bulk-like monoclinic stacking without rotation between layers, and  $a$  and  $b$  indicate the high-symmetry positions in the upper and lower layers, respectively. Shifts along [010] direction can result in non-monoclinic structures; however, we continue to use M for simplicity.

Figures 4 (a) and (b) show the energy difference among different stackings relative to the ground state energy for  $\text{FePS}_3$  and  $\text{NiPS}_3$ , respectively. Both systems exhibit similar behavior, with comparable local minima and global and local maxima. For  $\text{NiPS}_3$ ,  $M_P^{S_1}$  is the ground state, which is the bulk-type stacking; however, for  $\text{FePS}_3$ , the  $M_P^{F_e}$  stacking (P-3 point symmetry) is favored, being lower in energy by 9.42 meV/formula unit (f.u.) (see Fig. 4(a), insert figure). The dependence of the ground state on the metal atoms is also observed in other  $\text{TMPS}_3$ ; for example,  $\text{MnPS}_3$ , which presents  $M_P^P$  as the lower energy stacking [46]. Since we used the Hubbard U parameter to describe electron correlations in the 3d orbitals, we verified that different U values (see SM SIII for Hubbard-U = 4, 5, and 6 eV) yield consistent results regarding the difference in stackings. For the  $\text{FePS}_3$  system the binding energies, computed by the difference between the total energies of the optimized bilayer and monolayer,  $E_{BL} - 2E_{ML}$ , are -26.35 meV/f.u and -26.60 meV/f.u for  $M_P^{S_1}$  and  $M_P^{F_e}$  stacking, respectively, which is close to the average thermal energy at 300 K, indicating that

both stackings could be feasible at room temperature.

The shift of the layers relative to each other leads to a change in the interlayer distance (in the presence of lattice relaxation), as shown in Table 1 (where distance is defined as the difference in the z coordinates of the S atoms facing each other, see S2, SM). The main effect of the relaxation in the different stackings is a slight change in the distances between layers, which is typical for most 2D materials [47]. However, an exception occurs in the  $M_P^{S_4}$  stacking, where the layers are moved farther apart. This structural change is due to the strong S-S interlayer interaction, as the S atoms are positioned directly above one another (see S2, SM). This arrangement results in a strong Coulomb repulsion that surpasses the van der Waals interactions.

Furthermore, it is notable that  $\text{NiPS}_3$  exhibits a slightly larger interlayer distance compared to the  $\text{FePS}_3$  system. To discern the effects of structural distortions present in  $\text{FePS}_3$  and the intralayer distance on the stability of the  $M_P^{F_e}$  stacking over  $M_P^{S_1}$  in this system, we conducted frozen cell calculations for  $\text{FePS}_3$  using the relaxed structure of  $\text{NiPS}_3$ . This resulted in  $\text{FePS}_3$  having a nearly isotropic structure, similar to the comparison made between  $\text{FePS}_3$  and  $\text{MnPS}_3$  in Ref. [42]. In our case, the  $M_P^{F_e}$  stacking still exhibits lower energy by 11.18 and 8.75 meV per cell, considering the interlayer distances of  $d = 2.33 \text{ \AA}$  and  $2.40 \text{ \AA}$ , respectively. Hence, the stability of  $M_P^{F_e}$  remains independent of layer distances and M-S bond distortion.

Bulk  $\text{FePS}_3$  and  $\text{NiPS}_3$  exhibit AFM zigzag order within their layers and ferromagnetic or antiferromagnetic coupling between the layers [24]. We conducted calculations for different spin arrangements within each stacking to explore the stacking effect on the magnetic configuration between layers. For this purpose, we defined Configuration I (I) and Configuration II (II), with ferromagnetic and antiferromagnetic coupling (FMc and AFMc, respectively) between the first neighbors (see Fig. 1c, for bulk type,  $M_P^{S_1}$  stacking).

Fig. 4(d) shows the magnetic exchange energy, defined as the energy difference between the system in II and I ( $E_{II} - E_I$ ) [22]. As  $\delta$  increases along the [100] direction, an interplay between stacking and magnetic coupling is evident in both systems. In general, a local monotonic behavior is observed, where for small and large shifts, both systems favor AFMc and FMc between layers, respectively. One point of interest is the bulk-type stacking ( $M_P^{S_1}$ ) located at  $\delta = \frac{2}{3}$ . In this transition zone,  $\text{FePS}_3$  favors AFMc, with an energy difference  $\Delta E$  of -0.15 meV/Fe, while  $\text{NiPS}_3$  favors FMc, with a  $\Delta E$  of 0.25 meV/Ni.

The ionic relaxation slightly modifies the magnetic exchange energy for  $M_P^{S_1}$  and  $M_P^{F_e}$  (see Fig. 4(d)). However, for  $M_P^{S_4}$  stacking, the relaxed structures have the layers farther apart (see Table 1), resulting

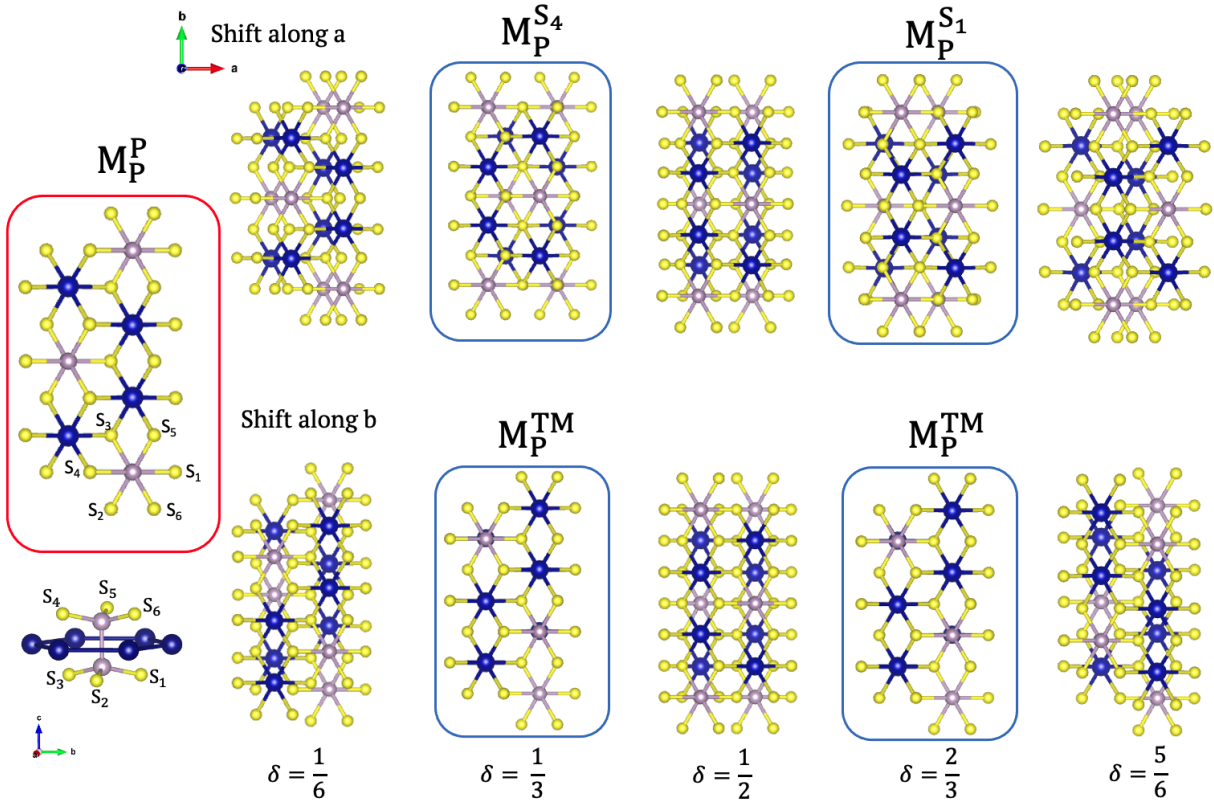


Figure 3: Bilayer structures for the  $\text{TMPS}_3$  systems under shift along  $\vec{a}$  (upper panel) and  $\vec{b}$  directions (lower panel). The relative shift correspond to  $\delta = \frac{1}{6}, \frac{1}{3}, \frac{1}{2}, \frac{2}{3}$  and  $\frac{5}{6}$ . The systems in the square box correspond to the high symmetry stackings.

in less Coulomb repulsion energy and decreasing exchange energy. For  $\delta$  along the  $[010]$  direction, a similar behavior is observed (see the discussion in the SM, Section SIV). Additionally, we have verified the robustness of the interlayer configuration by changing the distance between the layers (in the range  $d \pm 0.25\text{\AA}$ ).

Stacking (St)	$\text{FePS}_3$		$\text{NiPS}_3$	
	$\Delta E^{St}$ (meV/f.u.)	Distance ( $\text{\AA}$ ) $S_{\text{top}}, S_{\text{down}}$	$\Delta E^{St}$ (meV/f.u.)	Distance ( $\text{\AA}$ ) $S_{\text{top}}, S_{\text{down}}$
$M_P^{S1}$	6.98	2.33	0	2.37
$M_P^{TM}$	0	2.30	12.63	2.36
$M_P^P$	37.8	2.328	58.79	2.40
$M_P^{S4}$	344.57	2.820	335.36	2.81

Table 1: Stacking energy,  $\Delta E^{St}$ , for  $\text{FePS}_3$  and  $\text{NiPS}_3$  given by  $\Delta E^{St} = E^{St} - M_P^{TM}$  and  $E^{St} - M_P^{S1}$ , respectively (optimized structures).

The stacking dependence observed in  $\text{FePS}_3$  and  $\text{NiPS}_3$  offers an effective platform for studying the mechanism behind the magnetic coupling in  $\text{TMPS}_3$  systems.  $\text{FePS}_3$  and  $\text{NiPS}_3$  exhibit similar behavior, with the main difference being that  $\text{NiPS}_3$  displays a stronger magnetic exchange energy, indicating that it may host strong interlayer interactions, in agreement with experimental reports [25]. These differences arise from the different occupation of the  $3d$  states, leading

to distinct superexchange mechanisms. Figure 5 shows the density of states for each system. In  $\text{NiPS}_3$ , a gap opens between the  $e_g$  and  $t_{2g}$  states (fully occupied and almost degenerate). In  $\text{FePS}_3$ , the  $t_{2g}$  orbitals split, lowering the energy of the  $d_{xy}$  states while maintaining the degeneracy of the  $d_{xz}$  and  $d_{yz}$  orbitals. Additionally, the  $e_g$  states split. These results are consistent with previous experimental studies proposing that the  $t_{2g}$  states split into  $a_{1g}$  and  $eg_{\perp}$  states, defined as linear combinations of  $d_{xy}$ ,  $d_{yz}$ , and  $d_{xz}$  states [48]. However, this disagrees with theoretical calculations finding orbital ordering due to the occupation of  $d_{x^2-y^2}$  orbitals [49]. These differences may arise from the definition of the octahedra-axis reference, since the orbital projection in Ref. [49] is not made with octahedra aligned to the Cartesian coordinate system. In the next section, we will thus focus on understanding the exchange mechanism between the layers, mainly in the  $\text{NiPS}_3$  system – more details for  $\text{FePS}_3$  can be found in the SI.

### 3.1 Magnetic exchange

Our interest lies in stacking-dependent magnetism and understanding the mechanism behind the interplay between magnetic coupling and stacking. Therefore, we will focus on the interlayer exchange interaction ( $J^{inter}$ ), which can be determined by solving the effective clas-

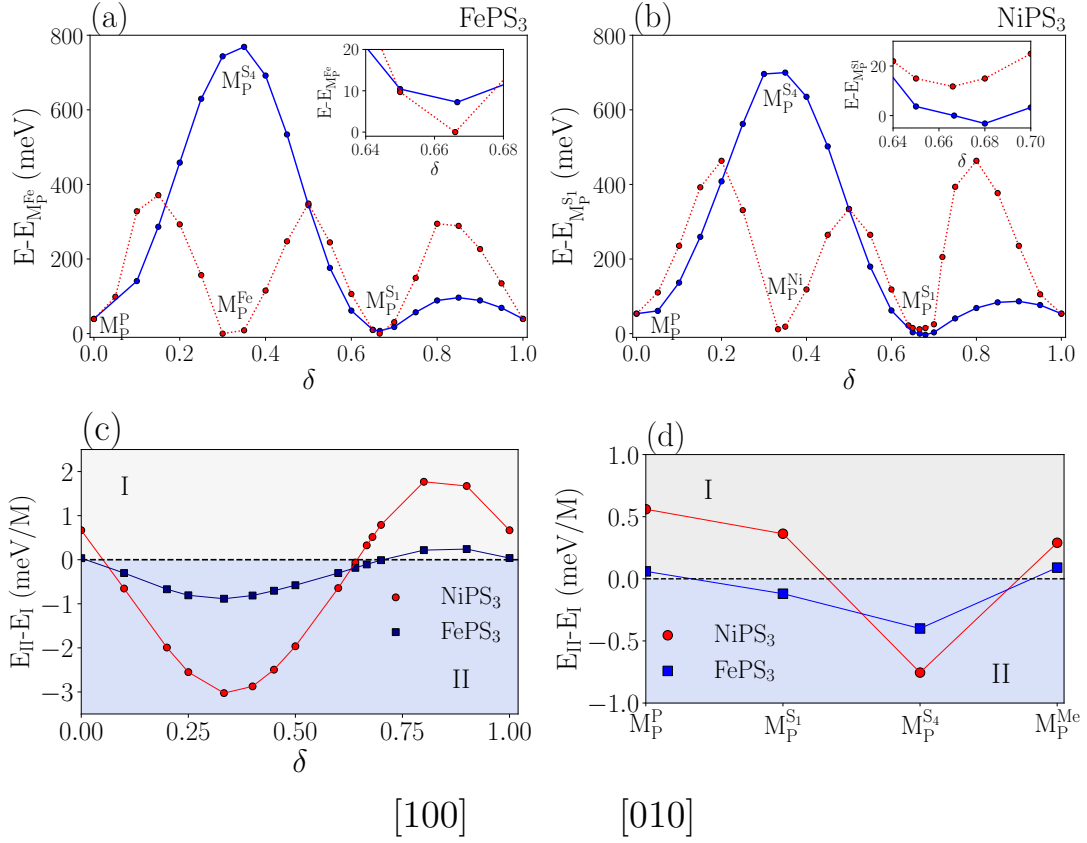


Figure 4: (a)-(b) Stacking energy as a function of lateral shift ( $\delta$ ) with respect to the ground state stacking  $M_P^{TM}$  and  $M_P^{S_1^i}$  for  $\text{FePS}_3$  and  $\text{NiPS}_3$ , respectively. The red and blue lines indicate the displacement along the  $[100]$  and  $[010]$  directions, respectively. (c) and (d) Total energy difference between configuration II and I (see Fig.1c) as a function  $\delta$  along  $[100]$  and for selected high symmetry stacking, respectively (optimized structures). FMC and AFMC mean regions with AFM and FM coupling, respectively.

sical Hamiltonian on a honeycomb lattice:

$$H = E_0 - \frac{1}{2} \sum_{i,j} J_{ij}^{intra} \vec{S}_i \cdot \vec{S}_j - \frac{1}{2} \sum_{i,j} J_{ij}^{inter} \vec{S}_i \cdot \vec{S}_j \quad (1)$$

where  $S_i$  is the total spin at atomic site  $i$ ,  $J_{ij}$  are the exchange coupling parameters between two local spins, and  $E_0$  is the total energy of the nonmagnetic state. We solve Eq. (1) for five magnetic configurations, considering the first three intralayer and interlayer neighbors for the lower-energy stackings ( $M_P^{S_1^i}$  and  $M_P^{Ni}$ ). The solutions for  $M_P^{S_1^i}$  stacking is given by:

$$\begin{aligned} E_{\text{Néel}} - E_0 &= \frac{NS^2}{2} (3J_1 - 6J_2 + 3J_3), \\ E_z^{I/II} - E_0 &= \frac{NS^2}{2} ((-J_1 + 2J_2 + 3J_3) \pm (-2J_4 + 2J_6)), \\ E_{z/\text{ferri}} - E_0 &= \frac{NS^2}{4} (-J_1 + 3J_3 - 2J_4 + 2J_6), \\ E_{s/\text{ferri}}^{I/II} - E_0 &= \frac{NS^2}{4} (J_1 - 3J_3 \pm (-2J_5 + 2J_6)), \\ E_{\text{ferri}}^I - E_0 &= \frac{NS^2}{2} (-2J_2 + J_4 + J_5), \end{aligned} \quad (2)$$

and for the  $M_P^{Ni}$  stacking by:

$$\begin{aligned} E_{\text{Néel}}^{I/II} - E_0 &= \frac{NS^2}{2} ((3J_1 - 6J_2 + 3J_3) \\ &\quad \pm \frac{1}{2}(-J_4 + 3J_5 - 6J_6)), \\ E_z^{I/II} - E_0 &= \frac{NS^2}{2} ((-J_1 + 2J_2 + 3J_3) \\ &\quad \pm \frac{1}{2}(-J_4 - J_5 + 2J_6)), \\ E_{s/\text{ferri}}^{II} - E_0 &= \frac{NS^2}{4} ((J_1 - 3J_3) \\ &\quad - (J_4 - J_5 - 2J_6)), \\ E_{z/\text{ferri}}^I - E_0 &= \frac{NS^2}{4} ((-J_1 + 3J_3) \\ &\quad - (J_4 + J_5 - 2J_6)), \\ E_{AFM-a} - E_0 &= \frac{NS^2}{2} ((-3J_1 - 6J_2 - 3J_3) \\ &\quad + \frac{1}{2}(J_4 + 9J_5 + 2J_6)), \end{aligned} \quad (3)$$

Here, I and II refer to Conf. I and Conf. II, respect-

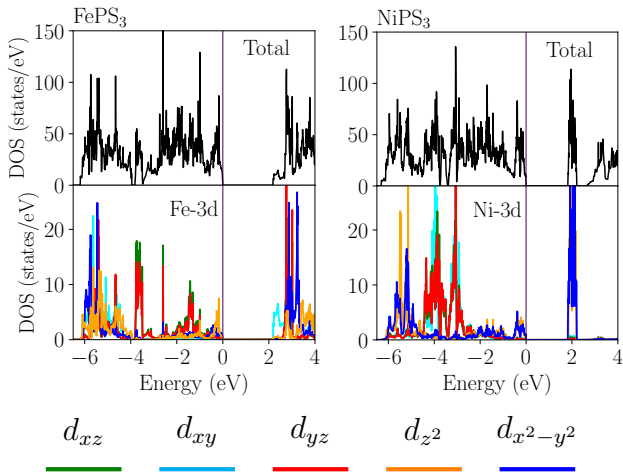


Figure 5: Density of states (DOS), total and projected to TM atoms for  $M_P^{S1}$  (bulk type stacking).

ively. The abbreviations z, s, ferri, and AFM-a stand for zigzag, stripy, ferrimagnetic (three atoms aligned ferromagnetically per unit cell), and a phase with two FM layers coupled antiferromagnetically (see Fig. 1(a)). Additionally, we have included various in-plane configurations that exhibit stabilities close to the zigzag configuration, such as zigzag-ferrimagnetic (z/ferri) and stripy-ferrimagnetic (s/ferri). SM Section SIV.1 provides further details about these configurations. Moreover,  $N$  is the total number of magnetic atoms per cell,  $S$  is the spin ( $S = 1$ ), and  $(J_1, J_2, J_3)$  and  $(J_4, J_5, J_6)$  correspond to the intralayer and interlayer magnetic exchange interactions, respectively (see, Fig. 7). The total energies for these configurations calculated with the relaxed structures of the zigzag-zigzag configuration are given in Table S4.

The  $M_P^{S1}$  stacking has two  $1^{st}$  and two  $2^{nd}$  NN, along with four  $3^{rd}$  NN interlayer exchange interactions (see Fig. 7). For the zigzag configuration, the magnetic interaction between the first NN determines the AFM/FM magnetic coupling between layers (see  $J_4$ , depicted in bi-lines in Fig. 7). In contrast, the second NN does not contribute due to spin frustration (see  $J_5$  depicted with solid line in Fig. 7). Moreover, the third NN contributes to both AFM and FM interactions. Therefore, for the zigzag configuration, both  $J_4$  and  $J_6$  contribute to Eq. (1) (see Eqs. (2),  $E_z^{I/II}$ ). However, the situation changes for other magnetic in-plane spin arrangements. For the Néel-Néel configuration, all interlayer NN are frustrated, resulting in no net interlayer exchange (see Eqs. (2),  $E_{Néel}$ ). In the case of stripy-ferri, the interaction with the first NN is frustrated ( $J_4$ ), and the interaction between the second and third NN dominates the magnetic exchange (see Eqs. (2),  $E_{s/ferri}$ ). Finally, the ferri configuration depends on the linear combination of  $J_4$  and  $J_5$  (see Eqs. (2),  $E_{ferri}$ ).

On the other hand, in the  $M_P^{TM}$  stacking, the A and B atoms in the honeycomb lattice of the metal atoms are no longer equivalent. For instance, in the zigzag-zigzag configuration (as shown in Fig. 7), the A atoms have one  $1^{st}$  NN, three  $2^{nd}$  and six  $3^{rd}$  NN (depicted with double red lines, a solid blue line and a dashed black line, respectively). In contrast, the B atoms have six  $2^{nd}$  NN, and the  $3^{rd}$  NN is beyond 8.7 Å; therefore, it is not considered. Unlike the  $M_P^{S1}$  stacking, the  $M_P^{TM}$  configuration does not exhibit frustration, regardless of the magnetic configuration. Therefore, the interlayer interactions depend on the linear combinations of  $J_4$ ,  $J_5$ , and  $J_6$  (see Eq.3).

The Ising model, which defines exchange parameters based on various magnetic configurations and distances between metal atoms while considering interactions with different neighbors, may overlook information related to interlayer interactions, where long-range distances have been shown to play a significant role [22, 23, 50]. In bilayer systems, neighboring atoms may have similar distances but follow different hopping paths, resulting in distinct couplings for the same separation. To account for these factors and provide a more comprehensive understanding of the relationship between Wannier orbitals and exchange parameters, we compute the exchange interactions by solving the Heisenberg Hamiltonian using the magnetic force theorem as implemented in the TB2J code [35].

Figure 6 (a-b) show the resulting intralayer and interlayer exchange terms solving Eqs. (2-3) and the derived with Heisenberg Hamiltonian. We find good agreement between both methods, with the exception of  $J_1$  (which we will refer to later). In both stackings, the predominant intralayer exchange interaction  $J^{intra}$  comes from the  $3^{rd}$  NNs at a distance of 6.75 Å. Our findings for  $J_2$  and  $J_3$  align with those reported in previous studies utilizing a Ising model [51] and real-space tight-binding Hamiltonian [20]. However, our calculated  $J_1 \sim 0.5$  meV, from the Heisenberg Hamiltonian, is lower than previously reported values [20]. This discrepancy likely arises from our inclusion of all intralayer  $J$  contributions without limiting them to the first three NN.

In NiPS<sub>3</sub>, the Ni ion with a Ni<sup>2+</sup> valence state, possesses eight valence electrons in the  $d$ -orbital shell. The  $t_{2g}$  orbitals are fully occupied in this electronic configuration, contributing predominantly to the lower energy states. In contrast, the  $e_g$  orbitals ( $d_{x^2-y^2}$  and  $d_{z^2}$ ) contribute mainly to the upper part of the conduction band, as illustrated in Fig. 5(b). Therefore, the exchange terms will be determined mainly by these orbitals.

For the intralayer magnetic exchange in both NiPS<sub>3</sub> stackings, the orbital-resolved interaction matrix shows that for the  $1^{st}$  NN, there is a weak direct magnetic interaction ( $J \sim 0.5$  meV) originating from the  $d_{x^2-y^2}$

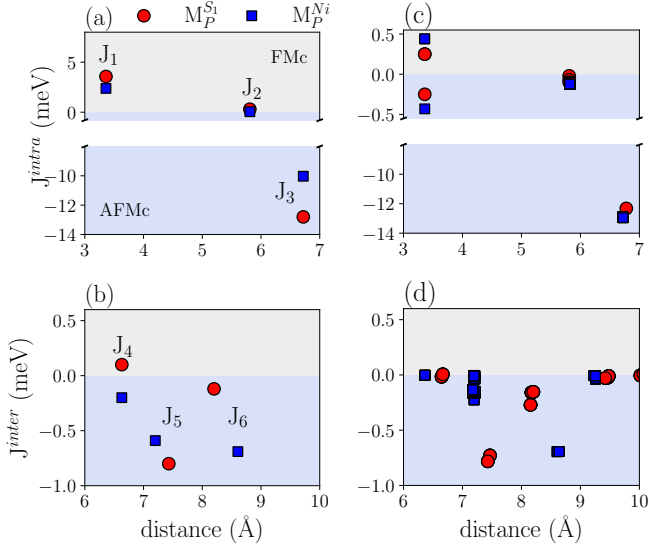


Figure 6: Magnetic exchange constants derived from the Ising Hamiltonian (Figs. (a-b)) and using the Magnetic Force Theorem as implemented in TB2J (Figs. (c-d)). Both models indicate that the interlayer magnetic exchange interaction is primarily contributed by the  $2^{nd}$  and  $3^{rd}$  nearest neighbors

and  $d_{z^2}$  orbitals. In contrast, for the  $2^{nd}$  NNs, there is no direct interaction, and SE mechanisms are disfavored due to the lack of alignment of  $S(p)$  orbitals, resulting in nearly zero exchange interactions. However, for the  $3^{rd}$  nearest neighbors (NNs), the alignment of  $Ni(d_{x^2-y^2})-S(p) \cdots S(p)-Ni(d_{x^2-y^2})$  orbitals favors the SE path, inducing a strong magnetic coupling of  $J_3 \approx -13$  meV per atom. In this case, for the  $M_P^{S1}$  system, the orbital-resolved interaction matrix is given by

$$J_3 \sim \begin{bmatrix} & J_{d_{xy}} & J_{d_{x^2-y^2}} & J_{d_{z^2}} \\ J_{d_{xy}} & -0.002 & -0.092 & 0.006 \\ J_{d_{x^2-y^2}} & -0.184 & -11.848 & -0.004 \\ J_{d_{z^2}} & 0.004 & 0.000 & -0.184 \end{bmatrix}, \quad (4)$$

similar results are obtained for the  $M_P^{Ni}$  stacking. The Wannier orbitals for the intralayer interaction are shown in the SM, [SIV.4](#).

In the case of the interlayer exchange terms, denoted as  $J^{inter}$ , different trends can be observed, where the interaction can favor either a AFM or weak FM coupling depending on the distance for Ising results (Fig. 6(b)). The  $M_P^{S1}$  stacking displays a weakly ferromagnetic coupling for the  $1^{st}$  NN located at  $6.75 \text{ \AA}$  ( $J_4$ ), with dominant magnetic interlayer interactions occurring at distances of  $7.5 \text{ \AA}$  and  $8.1 \text{ \AA}$ , corresponding to interaction strengths of approximately  $J_5 = -0.8$  meV ( $2^{nd}$  NN) and  $J_6 = -0.2$  meV ( $3^{rd}$  NN), respectively. However, a different trend is observed in  $M_P^{Ni}$ , where the strongest coupling occurs at around  $8.6 \text{ \AA}$  ( $J_6 = -0.7$  meV,  $3^{rd}$  NN). A similar trend is evident with the tight-binding

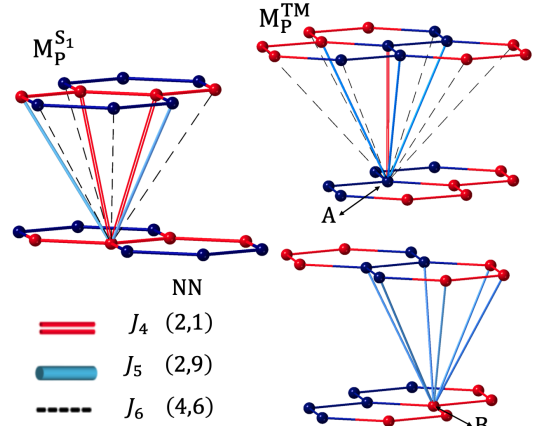


Figure 7: Figure shows the  $M_P^{S1}$  and  $M_P^{TM}$  stacking, respectively. It displays the bonds for first (red bi-lines), second (solid blue line), and third interlayer nearest neighbors (green dotted lines). In the case of  $M_P^{TM}$ , the interaction between the layers differs for the A and B atoms of the honeycomb lattice. Parenthesis numbers indicates the number of nearest neighbors (NN) for each stacking ( $M_P^{S1}$ ,  $M_P^{TM}$ ).

model, although it favored AFM coupling independent of the nearest neighbor. Here, we see that the main contribution to  $J$  comes from the  $2^{nd}$  NN for  $M_P^{S1}$  and the  $3^{rd}$  NN for  $M_P^{Ni}$ . Nevertheless, the interactions with the  $1^{st}$  NN are strongly suppressed in both stackings (Fig. 6(d)).

The strengthening of the magnetic exchange interaction between neighboring layers arises from the overlap of their orbitals through the super-superexchange interaction of  $Ni(d_{z^2})-S(p) \cdots S(p)-Ni(d_{z^2})$  and  $Ni(d_{x^2-y^2})-S(p) \cdots S(p)-Ni(d_{x^2-y^2})$  orbitals, resulting in an AFM nature, independent of the Ni coupling (AFM or FM). In the  $M_P^{S1}$  stacking configuration, the primary orbitals involved in the SE mechanism are the  $Ni(d_{x^2-y^2})$  orbitals, which exhibit strong hybridization with the  $S(p)$  orbitals (see SM, Fig. [SIV.4](#)). In the case of the  $1^{st}$  NN, the magnetic exchange interaction ( $J_4$ ) is notably weakened due to the misalignment of the sulfur atoms' p orbitals in the upper and down layers. Conversely, for the  $2^{nd}$  NN, the alignment of these p orbitals between layers strengthens the superexchange (SE) mechanism, resulting in a more favorable magnetic exchange ( $J_5 \sim -0.8$  meV) (see, Fig. 8). In the  $M_P^{Ni}$  stacking, we find that the magnetic interaction between the  $1^{st}$  and some of the  $2^{nd}$  NNs is strongly suppressed due to the lack of alignment of close S-S pairs. Moreover,  $J_6$  is enhanced because there are three possible interactions involving the  $d_{x^2-y^2}$  and  $d_{z^2}$  orbitals at a distance of approximately  $8.7 \text{ \AA}$ .

The observed trend for the interlayer exchange interaction in  $NiPS_3$  aligns with behaviors observed in other van der Waals magnets. Previous studies have shown that the primary contribution to interlayer exchange can originate from atom pairs located at dis-

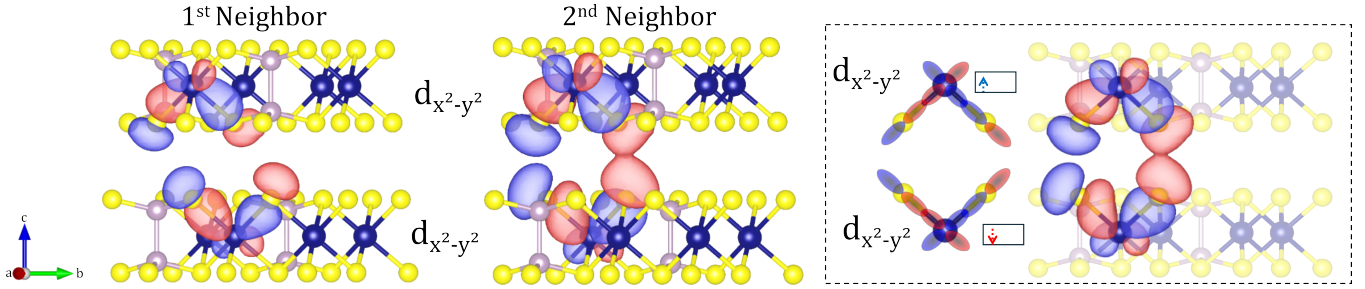


Figure 8: Localized Wannier orbitals for NiPS<sub>3</sub>,  $M_P^{S1}$  stacking, for 1<sup>st</sup> and 2<sup>nd</sup> interlayer neighbors. For the 1<sup>st</sup> interlayer neighbors, there is no alignment between the p orbitals of the sulfur atoms in the upper and down layers, which happens with the 2<sup>nd</sup> interlayer neighbors. The right diagram shows a schematic representation of the interaction between 2<sup>nd</sup> interlayer neighbors. (Iso-surperic with a value equal to 2.6).

tances longer than the first nearest neighbors. For instance, in compounds such as CrX<sub>3</sub> (X = Cl [52], Br [50] and I [23]), the strongest interlayer exchange can arise from either first or second neighbors, depending on the stacking configuration which in turn depends on SE mechanisms.

In the case of FePS<sub>3</sub>, we have detected some inconsistencies when comparing our Ising results with the tight-binding model based on WF analysis. By solving Eqs. (2), we found that all interlayer interactions favor AFM coupling, with  $J_5 \sim J_3$  (see further details in SM Table S1). However, we also found that the strength of the interlayer exchange constants strongly depends on the magnetic configurations used to calculate them. In our tight-binding model analysis for bulk-type stacking, we obtained the same sign for all magnetic couplings (intralayer and interlayer), which contradicts the zigzag magnetic order. Due to the electronic structure of FePS<sub>3</sub>, which includes singly-occupied  $d_{xz}/d_{yz}$  and  $e_g$  orbitals (see Fig. 5), we anticipate a strong competition between ferromagnetic and antiferromagnetic interlayer interactions. This competition involves a combination of several orbital channels, which could result in weaker interlayer interactions. This scenario could explain the weak exchange energy observed in this system compared to NiPS<sub>3</sub> (see Fig. 4(c-d)).

In summary, our study provides valuable insights into the interlayer magnetic interactions and stacking preferences in NiPS<sub>3</sub> and FePS<sub>3</sub> bilayers. NiPS<sub>3</sub> displays a weak AFM interaction between the  $d_{x^2-y^2}$  and  $d_{z^2}$  orbitals of the 1<sup>st</sup> NNs. The main interaction comes from the 2<sup>nd</sup> or 3<sup>rd</sup> NNs depending on the stacking, since the alignment of the sulfur orbitals of the two layers provides an SE interaction path, analog to the process that happens on the 3<sup>rd</sup> NN intralayer interaction [20].

In case of FePS<sub>3</sub>, our results suggest that antiferromagnetic coupling between layers is more energetically favorable for the  $M_P^{S1}$  (bulk-type stacking), in contrast,  $M_P^{Fe}$  stacking favors ferromagnetic coupling. Although our findings align with experimental reports of the magnetic ground state in bulk-type stacking, the lowest energy stacking corresponds to the  $M_P^{Fe}$  configuration. We

observed a strong interplay between the stacking and magnetic configurations in both NiPS<sub>3</sub> and FePS<sub>3</sub> systems, which also depend on intralayer magnetic configurations.

Our studies indicate the potential tunability of magnetic coupling through stacking shifts in NiPS<sub>3</sub>, making it relevant for exploring TMPS<sub>3</sub> moiré systems. Unlike Fe, Ni has strong magnetic exchange coupling for high-symmetry stacking. Therefore, neutron spectroscopy could detect changes in their magnetic configuration with stacking. The ability to control magnetic interactions in differently stacked regions opens up intriguing possibilities, particularly in emergent magnetic textures, spin polarization, or even the formation of skyrmions. Exploring TMPS<sub>3</sub> moiré structures could be an avenue to manipulate magnetic order and optical properties in 2D antiferromagnets, and could potentially lead to the exploration of altermagnetic phases as recently suggested [53]. There is still much to investigate in TMPS<sub>3</sub> systems, and our study took the first step by conducting a theoretical analysis of the magnetic interactions in stacked antiferromagnetic bilayer systems.

## 4 Acknowledgments

We thank Efrat Lifshitz, Magdalena Birowska and Jhon Gonzalez for fruitful discussions. The authors gratefully acknowledge the computing time made available to them on the high-performance computer at the NHR Center of TU Dresden and on the high-performance computers Noctua 2 at the NHR Center PC2. These are funded by the German Federal Ministry of Education and Research and the state governments participating on the basis of the resolutions of the GWK for the national high-performance computing at universities ([www.nhr-verein.de/unsere-partner](http://www.nhr-verein.de/unsere-partner)). A.L. thanks to Chilean FONDECYT Postdoctoral Grant No. 3220505. We would like to thank the German Science Foundation (DFG) for supporting this work with the DIP grant No.1223-21. BC acknowledges financial support by the DFG via the SFB 1415, Project ID No. 417590517.



## References

- [1] Hongchao Xie, Xiangpeng Luo, Gaihua Ye, Zhipeng Ye, Haiwen Ge, Suk Hyun Sung, Emily Rennich, Shaohua Yan, Yang Fu, Shangjie Tian, et al. Twist engineering of the two-dimensional magnetism in double bilayer chromium triiodide homostructures. *Nature Physics*, 18(1):30–36, 2022.
- [2] Doried Ghader. Magnon magic angles and tunable Hall conductivity in 2D twisted ferromagnetic bilayers. *Scientific Reports*, 10(1):15069, 2020.
- [3] Sharidya Rahman, Juan F Torres, Ahmed Raza Khan, and Yuerui Lu. Recent developments in van der Waals antiferromagnetic 2D materials: Synthesis, characterization, and device implementation. *ACS Nano*, 15(11):17175–17213, 2021.
- [4] Soonmin Kang, Kangwon Kim, Beom Hyun Kim, Jonghyeon Kim, Kyung Ik Sim, Jae-Ung Lee, Sungmin Lee, Kisoo Park, Seokhwan Yun, Taehun Kim, Abhishek Nag, Andrew Walters, Mirian Garcia-Fernandez, Jiemin Li, Laurent Chapon, Ke-Jin Zhou, Young-Woo Son, Jae Hoon Kim, Hyeonsik Cheong, and Je-Geun Park. Coherent many-body exciton in van der Waals antiferromagnet NiPS<sub>3</sub>. *Nature*, 583:785–789, 2020.
- [5] Maria Ramos, Francisco Marques-Moros, Dorye L Esteras, Samuel Mañas-Valero, Eudomar Henríquez-Guerra, Marcos Gadea, José J Baldoví, Josep Canet-Ferrer, Eugenio Coronado, and M Reyes Calvo. Photoluminescence Enhancement by Band Alignment Engineering in MoS<sub>2</sub>/FePS<sub>3</sub> van der Waals Heterostructures. *ACS Applied Materials & Interfaces*, 14(29):33482–33490, 2022.
- [6] M Bora and P Deb. Magnetic proximity effect in two-dimensional van der waals heterostructure. *Journal of Physics: Materials*, 4(3):034014, 2021.
- [7] title = Two-dimensional transition metal phosphorous trichalcogenides (MPX<sub>3</sub>): a review on emerging trends, current state and future perspectives Samal, Rutuparna and Sanyal, Gopal and Chakraborty, Brahmananda and Rout, Chandra Sekhar. *Journal of Material Chemistry A*, 9:2560–2591, 2021.
- [8] Wenyu Xing, Luyi Qiu, Xirui Wang, Yunyan Yao, Yang Ma, Ranran Cai, Shuang Jia, X. C. Xie, and Wei Han. Magnon transport in quasi-two-dimensional van der waals antiferromagnets. *Physical Review X*, 9:011026, 2019.
- [9] Xingzhi Wang, Kezhao Du, Yu Yang Fredrik Liu, Peng Hu, Jun Zhang, Qing Zhang, Man Hon Samuel Owen, Xin Lu, Chee Kwan Gan, Pinaki Sengupta, Christian Kloc, and Qihua Xiong. Raman spectroscopy of atomically thin two-dimensional magnetic iron phosphorus trisulfide (FePS<sub>3</sub>) crystals. *2D Materials*, 3:031009, 2016.
- [10] A R Wildes, V Simonet, E Ressouche, R Ballou, and G J McIntyre. The magnetic properties and structure of the quasi-two-dimensional antiferromagnet CoPS<sub>3</sub>. *Journal of Physics: Condensed Matter*, 29:455801, 2017.
- [11] Maria Ramos, Felix Carrascoso, Riccardo Frisenda, Patricia Gant, Samuel Mañas-Valero, Dorye L Esteras, José J Baldoví, Eugenio Coronado, Andres Castellanos-Gomez, and M Reyes Calvo. Ultra-broad spectral photo-response in FePS<sub>3</sub> air-stable devices. *npj 2D Materials and Applications*, 5(1):19, 2021.
- [12] Jan Wyzula, Ivan Mohelsky, Diana Václavková, Piotr Kapuscinski, Martin Veis, Clément Faugeras, Marek Potemski, Mike E Zhitomirsky, and Milan Orlita. High-angular momentum excitations in collinear antiferromagnet FePS<sub>3</sub>. *Nano Letters*, 22(23):9741–9747, 2022.
- [13] Thuc T Mai, Kevin F Garrity, Amber McCreary, Joshua Argo, Jeffrey R Simpson, Vicky Doan-Nguyen, Rolando Valdés Aguilar, and Angela R Hight Walker. Magnon-phonon hybridization in 2D antiferromagnet MnPSe<sub>3</sub>. *Science Advances*, 7(44):eabj3106, 2021.
- [14] Christopher Lane and Jian-Xin Zhu. Thickness dependence of electronic structure and optical properties of a correlated van der Waals antiferromagnetic NiPS<sub>3</sub> thin film. *Physical Review B*, 102(7):075124, 2020.
- [15] Danyun Xu, Zhe Guo, Yudi Tu, Xinzhe Li, Yu Chen, Zhesheng Chen, Bingbing Tian, Shuqing Chen, Yumeng Shi, Ying Li, Chenliang Su, and Dianyuan Fan. Controllable nonlinear optical properties of different-sized iron phosphorus trichalcogenide (FePS<sub>3</sub>) nanosheets. *Nanophotonics*, 9:4555–4564, 2020.
- [16] Kangwon Kim, Soo Yeon Lim, Jae-Ung Lee, Sungmin Lee, Tae Yun Kim, Kisoo Park, Gun Sang Jeon, Cheol-Hwan Park, Je-Geun Park, and Hyeonsik Cheong. Suppression of magnetic ordering in XXZ-type antiferromagnetic monolayer NiPS<sub>3</sub>. *Nature Communications*, 10(1):345, 2019.
- [17] Mouhui Yan, Yichen Jin, Zhicheng Wu, Arshak Tsaturyan, Anna Makarova, Dmitry Smirnov, Elena Voloshina, and Yuriy Dedkov. Correlations in the electronic structure of van der Waals NiPS<sub>3</sub> crystals: An x-ray absorption and resonant photoelectron spectroscopy study. *The Journal of Physical Chemistry Letters*, 12(9):2400–2405, 2021.

- [18] Juanmei Duan, Phanish Chava, Mahdi Ghorbani-Asl, Denise Erb, Liang Hu, Arkady V Krashe-ninnikov, Harald Schneider, Lars Rebohle, Ar-tur Erbe, Manfred Helm, et al. Enhanced trion emission in monolayer MoSe<sub>2</sub> by constructing a type-I van der Waals heterostructure. Advanced Functional Materials, 31(40):2104960, 2021.
- [19] Bheema Lingam Chittari, Youngju Park, Dongkyu Lee, Moon-sup Han, Allan H MacDonald, Euyheon Hwang, and Jeil Jung. Electronic and magnetic properties of single-layer MPX<sub>3</sub> metal phosphor-ous trichalcogenides. Physical Review B, 94(18): 184428, 2016.
- [20] Carmine Autieri, Giuseppe Cuono, Canio Noce, Milosz Rybak, Kamila M Kotur, Cliò Efthimia Agrapidis, Krzysztof Wohlfeld, and Magdalena Birowska. Limited ferromagnetic interactions in monolayers of MPS<sub>3</sub> (M= Mn and Ni). Physical Chemistry C, 126(15):6791–6802, 2022.
- [21] Tae Yun Kim and Cheol-Hwan Park. Magnetic anisotropy and magnetic ordering of transition-metal phosphorus trisulfides. Nano Letters, 21(23): 10114–10121, 2021.
- [22] Nikhil Sivadas, Satoshi Okamoto, Xiaodong Xu, Craig J Fennie, and Di Xiao. Stacking-dependent magnetism in bilayer CrI<sub>3</sub>. Nano Letters, 18(12): 7658–7664, 2018.
- [23] Seung Woo Jang, Min Yong Jeong, Hongkee Yoon, Siheon Ryee, and Myung Joon Han. Microscopic understanding of magnetic interactions in bilayer CrI<sub>3</sub>. Physical Review Materials, 3(3):031001, 2019.
- [24] Hao Chu, Chang Jae Roh, Joshua O Island, Chen Li, Sungmin Lee, Jingjing Chen, Je-Geun Park, Andrea F Young, Jong Seok Lee, and David Hsieh. Linear magnetoelectric phase in ultrathin MnPS<sub>3</sub> probed by optical second harmonic generation. Physical Review Letters, 124(2):027601, 2020.
- [25] Xiaoli Ma, Yimeng Wang, Yunyu Yin, Binbin Yue, Jianhong Dai, Jinguang Cheng, Jianting Ji, Feng Jin, Fang Hong, Jian-Tao Wang, et al. Dimensional crossover tuned by pressure in layered mag-netic NiPS<sub>3</sub>. Science China Physics, Mechanics & Astronomy, 64(9):297011, 2021.
- [26] Sihan Yan, Cheng Wang, Qiyun Xie, Limin Chen, Wei Wang, and Xiaoqian Ai. Layer-dependent Ra-man spectroscopy study on two-dimensional van der Waals antiferromagnetic semiconductor MPS<sub>3</sub> (M= Fe, Mn). Solid State Communications, 348: 114764, 2022.
- [27] John P. Perdew, Kieron Burke, and Matthias Ernzerhof. Generalized gradient approximation made simple. Physical Review Letters, 77:3865–3868, Oct 1996.
- [28] G. Kresse and D. Joubert. From ultrasoft pseudopotentials to the projector augmented-wave method. Physical Review B, 59:1758–1775, 1999.
- [29] Jiří Klimeš, David R. Bowler, and Angelos Mi-chaelides. Van der waals density functionals ap-plied to solids. Physical Review B, 83(19):195131, 2011.
- [30] Ramesh Naidu Jenjeti, Rajat Kumar, Muthu P Austeria, and S Sampath. Field effect transistor based on layered NiPS<sub>3</sub>. Scientific Reports, 8(1): 8586, 2018.
- [31] Sebastian Pazek, Anna Efimenko, Roberto Félix, Maria Roslova, Christine Joy Querebillo, Mikhail V Gorbunov, Alexander Ovchinnikov, Andreas Koitzsch, Carlos Escudero, Yuliia Shemer-liuk, et al. Charge compensation in a layered van der Waals NiPS<sub>3</sub> host through various cationic intercalations. Journal of Materials Chemistry A, 12(6):3523–3541, 2024.
- [32] Fatemeh Haddadi, Edward Linscott, Iurii Timrov, Nicola Marzari, and Marco Gibertini. On-site and intersite Hubbard corrections in magnetic mono-layers: The case of FePS<sub>3</sub> and CrI<sub>3</sub>. Physical Review Materials, 8(1):014007, 2024.
- [33] Sergei L Dudarev, Gianluigi A Botton, Sergey Y Savrasov, CJ Humphreys, and Adrian P Sutton. Electron-energy-loss spectra and the structural sta-bility of nickel oxide: An LSDA+ U study. Physical Review B, 57(3):1505, 1998.
- [34] D. J. Chadi. Special points for brillouin-zone in-tegrations. Physical Review B, 16(4):1746–1747.
- [35] Xu He, Nicole Helbig, Matthieu J Verstraete, and Eric Bousquet. TB2J: A python package for com-puting magnetic interaction parameters. Computer Physics Communications, 264:107938, 2021.
- [36] Giovanni Pizzi, Valerio Vitale, Ryotaro Ar-ita, Stefan Blügel, Frank Freimuth, Guillaume Géranton, Marco Gibertini, Dominik Gresch, Charles Johnson, Takashi Koretsune, Julen Ibañez-Azpiroz, Hyungjun Lee, Jae-Mo Lihm, Daniel Marchand, Antimo Marrazzo, Yuriy Mokrousov, Jamal I Mustafa, Yoshiro Nohara, Yusuke Nomura, Lorenzo Paulatto, Samuel Poncé, Thomas Pon-weiser, Junfeng Qiao, Florian Thöle, Stepan S Tsirkin, Małgorzata Wierzbowska, Nicola Marzari, David Vanderbilt, Ivo Souza, Arash A Mostofi, and Jonathan R Yates. Wannier90 as a community code: new features and applications. Journal of Physics: Condensed Matter, 32:165902, 2020.

- [37] Kyle Hwangbo, Qi Zhang, Qianni Jiang, Yong Wang, Jordan Fonseca, Chong Wang, Geoffrey M Diederich, Daniel R Gamelin, Di Xiao, Jiun-Haw Chu, et al. Highly anisotropic excitons and multiple phonon bound states in a van der waals antiferromagnetic insulator. Nature Nanotechnology, 16(6):655–660, 2021.
- [38] Andrew R Wildes, Virginie Simonet, Eric Ressouche, Garry James McIntyre, Maxim Avdeev, Emmanuelle Suard, Simon AJ Kimber, Diane Lançon, Giulio Pepe, Boujemaa Moubaraki, et al. Magnetic structure of the quasi-two-dimensional antiferromagnet NiPS<sub>3</sub>. Physical Review B, 92(22):224408, 2015.
- [39] Carina A Belvin, Edoardo Baldini, Ilkem Ozge Ozel, Dan Mao, Hoi Chun Po, Clifford J Allington, Suhan Son, Beom Hyun Kim, Jonghyeon Kim, Inho Hwang, et al. Exciton-driven antiferromagnetic metal in a correlated van der waals insulator. Nature Communications, 12(1):4837, 2021.
- [40] Jae-Ung Lee, Sungmin Lee, Ji Hoon Ryoo, Soonmin Kang, Tae Yun Kim, Pilkwang Kim, Cheol-Hwan Park, Je-Geun Park, and Hyeonsik Cheong. Ising-type magnetic ordering in atomically thin FePS<sub>3</sub>. Nano Letters, 16(12):7433–7438, 2016.
- [41] D Lançon, HC Walker, Eric Ressouche, B Oulad-diaf, KC Rule, GJ McIntyre, TJ Hicks, Henrik M Rønnow, and AR Wildes. Magnetic structure and magnon dynamics of the quasi-two-dimensional antiferromagnet FePS<sub>3</sub>. Physical Review B, 94(21):214407, 2016.
- [42] Ellenor Geraffly, Shahar Zuri, Milosz Marcin Rybak, Faris Horani, Adam K Budniak, Yaron Amouyal, Magdalena Birowska, and Efrat Lifshitz. Crystal anisotropy implications on the intrinsic magnetic and optical properties in van der Waals FePS<sub>3</sub>. arXiv preprint arXiv:2208.10890, 2022.
- [43] Chisato Murayama, Momoko Okabe, Daisuke Urushihara, Toru Asaka, Koichiro Fukuda, Masahiko Isobe, Kazuo Yamamoto, and Yoshitaka Matsushita. Crystallographic features related to a van der Waals coupling in the layered chalcogenide FePS<sub>3</sub>. Journal of Applied Physics, 120(14), 2016.
- [44] Dmytro Afanasiev, Jorrit R Hortensius, Matthias Matthiesen, Samuel Mañas-Valero, Makars Šiškins, Martin Lee, Edouard Lesne, Herre SJ van Der Zant, Peter G Steeneken, Boris A Ivanov, et al. Controlling the anisotropy of a van der waals antiferromagnet with light. Science Advances, 7(23):eabf3096, 2021.
- [45] Hongyi Yu, Gui-Bin Liu, and Wang Yao. Brightened spin-triplet interlayer excitons and optical selection rules in van der waals heterobilayers. 2D Materials, 5(3):035021, 2018.
- [46] Xiao Li, Ting Cao, Qian Niu, Junren Shi, and Ji Feng. Coupling the valley degree of freedom to antiferromagnetic order. Proceedings of the National Academy of Sciences, 110(10):3738–3742, 2013.
- [47] Wei Li, Thomas Brumme, and Thomas Heine. Relaxation effects in transition metal dichalcogenide bilayer heterostructures. npj 2D Materials and Applications, 8(1):43, 2024.
- [48] Aldrin G Chang, Liang-Wei Lan, Yao-Jui Chan, Chia-Nung Kuo, Ting Chen, Chih-Heng Huang, Tzu-Hung Chuang, Der-Hsin Wei, Chin-Shan Lue, and Chien-Cheng Kuo. Trigonal distortion in zigzag-antiferromagnet iron phosphorus trisulfide. Physical Review B, 106(12):125412, 2022.
- [49] Mohammad Amirabbasi and Peter Kratzer. Orbital and magnetic ordering in single-layer FePS<sub>3</sub>: A DFT+ U study. Physical Review B, 107(2):024401, 2023.
- [50] Jun-Shan Si, Hongxing Li, Bin-Guang He, Zi-Peng Cheng, and Wei-Bing Zhang. Revealing the underlying mechanisms of the stacking order and interlayer magnetism of bilayer CrBr<sub>3</sub>. The Journal of Physical Chemistry C, 125(13):7314–7320, 2021.
- [51] Thomas Olsen. Magnetic anisotropy and exchange interactions of two-dimensional FePS<sub>3</sub>, NiPS<sub>3</sub> and MnP<sub>3</sub>S from first principles calculations. Journal of Physics D: Applied Physics, 54(31):314001, 2021.
- [52] Ali Ebrahimian, Anna Dyrdał, and Alireza Qaiumzadeh. Control of magnetic states and spin interactions in bilayer CrCl<sub>3</sub> with strain and electric fields: an ab initio study. Scientific Reports, 13(1):5336, 2023.
- [53] Yichen Liu, Junxi Yu, and Cheng-Cheng Liu. Twisted magnetic van der waals bilayers: An ideal platform for altermagnetism. arXiv preprint arXiv:2404.17146, 2024.
- [54] Qinghua Liang, Yun Zheng, Chengfeng Du, Yubo Luo, Jianli Zhang, Bing Li, Yun Zong, and Qingyu Yan. General and scalable solid-state synthesis of 2D MPS<sub>3</sub> (M= Fe, Co, Ni) nanosheets and tuning their Li/Na storage properties. Small Methods, 1(12):1700304, 2017.
- [55] Adam K Budniak, Szymon J Zelewski, Magdalena Birowska, Tomasz Woźniak, Tatyana Bendikov, Yaron Kauffmann, Yaron Amouyal, Robert Kudrawiec, and Efrat Lifshitz. Spectroscopy and Structural Investigation of Iron Phosphorus Trisulfide—FePS<sub>3</sub>. Advanced Optical Materials, 10(7):2102489, 2022.

**Supplemental Material:**  
**Interlayer Magnetic Coupling in FePS<sub>3</sub> and NiPS<sub>3</sub> Stacked Bilayer**

Andrea León,<sup>1,4</sup> Beatriz Costa,<sup>2,3</sup> Thomas Heine,<sup>2,3,4,5</sup> Thomas Brumme<sup>4</sup>

<sup>1</sup>Departamento de Física, Facultad de Ciencias, Universidad de Chile, Casilla 653, Santiago, Chile.

<sup>2</sup>Helmholtz-Zentrum Dresden-Rossendorf, Bautzner Landstr. 400, 01328 Dresden, Germany.

<sup>3</sup>Center for Advanced Systems Understanding, CASUS, Untermarkt 20, 02826 Görlitz, Germany.

<sup>4</sup>Chair of Theoretical Chemistry, Technische Universität Dresden, Bergstrasse 66, 01069 Dresden, Germany.

<sup>5</sup>Yonsei University and ibs-cnms, Seodaemun-gu, Seoul 120-749, Republic of Korea.

18th October 2024

## SI Wannier functions

We employed Wannier localized functions for the tight-binding model, constructing the Wannier Hamiltonian with the d orbitals of the metal atoms and the p orbitals of the sulfur atoms. The localization of these functions was verified by examining the ratio between the real and imaginary components of the orbitals, ensuring it was close to zero. Additionally, we confirmed the alignment between the DFT and Wannier band structures and evaluated the orbital spreads, which were less than 1 Å for the d orbitals and less than 2 Å for the p orbitals. During the Wannierization process, 10,000 steps were conducted to ensure proper localization, although maximally localized Wannier functions were not utilized. The magnetic interactions were calculated using the TB2J code, which employs the Green's function method with local rigid spin rotation treated as a perturbation to derive the exchange parameters. For orbital analysis, the system was rotated so that the octahedra formed by the metal and sulfur atoms were aligned with the Cartesian axes, meaning the layers were not perpendicular to the z-axis.

## SII (Fe,Ni)PS<sub>3</sub> Bulk

	$a$ (Å)	$b$ (Å)	$c$ (Å)	$d_L$ (Å)
NiPS <sub>3</sub> -Computed	5.81	10.09	6.62	6.32
NiPS <sub>3</sub> -Experiment	5.80 [54]	10.03 [54]	6.60 [54]	6.34 [31]
FePS <sub>3</sub> -Computed	5.98	10.30	6.73	6.45
FePS <sub>3</sub> -Experiment	5.95 [55]	10.30 [55]	6.72 [55]	~ 6.40 [26]

Table S1: Lattice parameter and layer distance ( $d_L$ ).

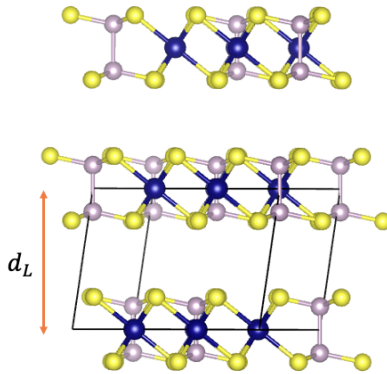


Figure S1: FePS<sub>3</sub> and NiPS<sub>3</sub> Bulk.

## SIII Bilayer stability as Hubbard-U parameter

Table S2 shows the energy difference between the lowest energy stackings ( $M_P^{S1}$  and  $M_P^{TM}$  for FePS<sub>3</sub> and NiPS<sub>3</sub> system, respectively) for several Hubbard-U values  $U = 4, 5$  and  $6$  eV. Hence, the lowest energy stacking is independent of the  $U$  value in the explored range.

Stackings	FePS <sub>3</sub>			NiPS <sub>3</sub>		
	$\Delta E$ (meV), U = 4 eV	$\Delta E$ (meV), U = 5 eV	$\Delta E$ (meV), U = 6 eV	$\Delta E$ (meV), U = 4 eV	$\Delta E$ (meV), U = 5 eV	$\Delta E$ (meV), U = 6 eV
$M_P^{S_1}$	10.18	6.98	7.95	0	0	0
$M_P^{TM}$	0	0	0	14.56	12.63	10.95

Table S2: Energy difference between the  $M_P^{TM}$  and  $M_P^{S_1}$  stackings, for Fe and Ni, considering three Hubbard-U values (U = 4, 5, and 6 eV).

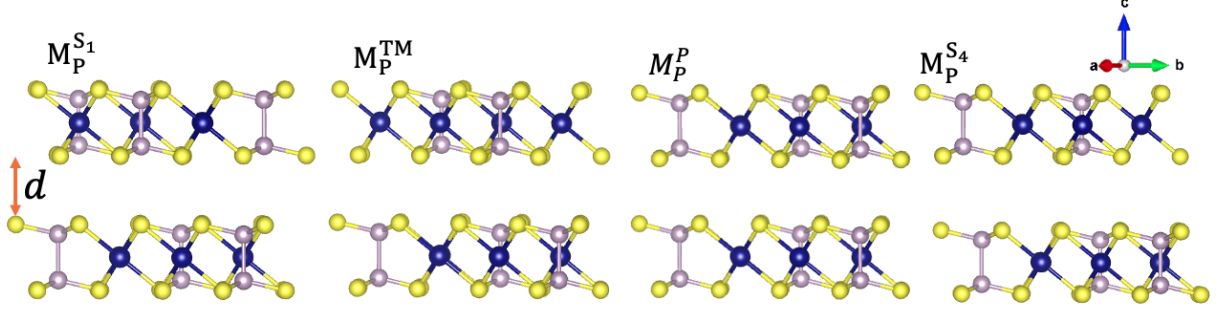


Figure S2: Front view of selected high symmetry stacking. “ $d$ ” is the distance between  $S^{top}$ - $S^{down}$  layers.

## SIV Magnetic configuration

Figure S3(a)-(b) upper panel illustrates the energy stacking due to a shift by  $\delta$  along the [010] direction for FePS<sub>3</sub> and NiPS<sub>3</sub>, respectively. The lower panel displays the energy differences between Conf.II and Conf.I. (Conf.I and Conf.II correspond to FM and AFM respectively, as shown in Fig. S3(c)).

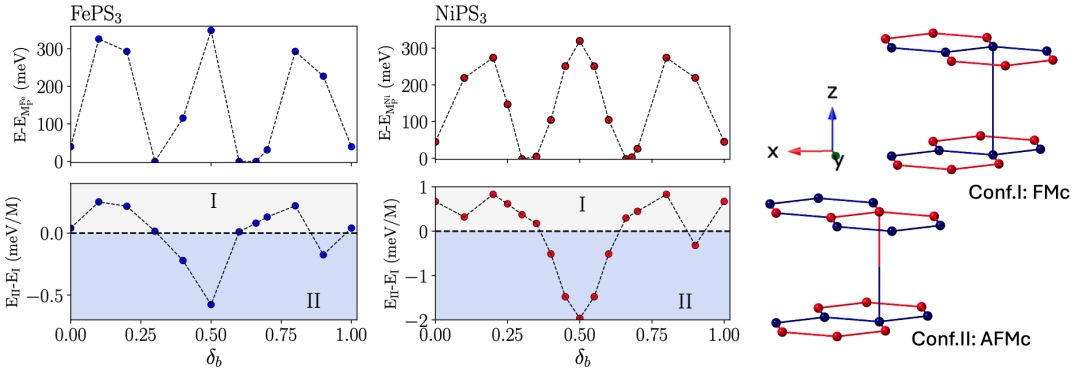


Figure S3: Upper panel: Stacking energy as a function of the shift along the  $b$ -direction. Lower panel displays the energy difference between Conf.II (II) and Conf.I (I), which represent two possible magnetic couplings between the layers (see Fig. (c)), defined as antiferromagnetic and ferromagnetic interactions among first neighbors in  $M_P^M$  stacking ( $\delta = 2/3$ ).

### SIV.1 Interplay between in plane and interlayer configurations

We explored different magnetic configurations such as Néel, stripy, and FM, all of which have already been investigated in monolayer structures. Additionally, we included combinations of these magnetic configurations based on zigzag-configurations, such as zigzag-Néel, zigzag-stripy, and zigzag-ferrimagnetic (ferri) (see Fig. S4). Table S3 shows the energy differences among the different configurations for Fe and Ni systems with  $M_P^{S_1}$  (bulk-type stacking). For both systems, zigzag has the lowest configuration energy, as expected. However, we found that the zigzag-Néel configuration follows as the next metastable state, followed by configurations with higher energy such as Néel, zig-stripy, and zig-ferrimagnetic configurations. Additionally, we observed that the stripy configuration is the most unfavorable state. However, when combined with zigzag, this configuration gains stability. Other mixed magnetic configurations based on the Néel-configuration are metastable states with higher energy. Interestingly, we observed that the combining zigzag with ferrimagnetic coupling is much more favorable than other antiferromagnetic configurations,

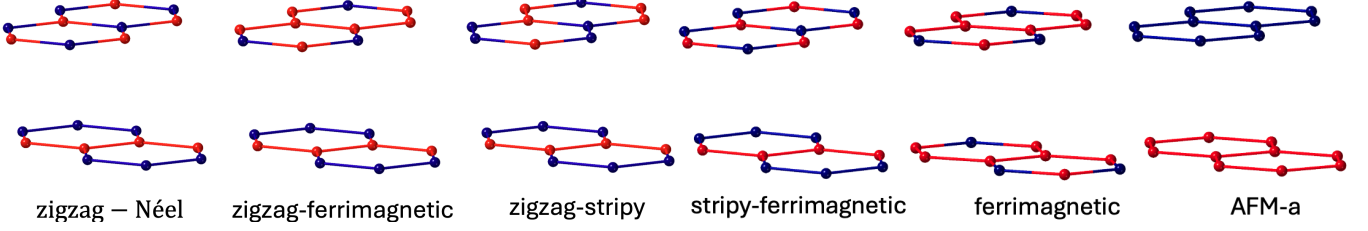


Figure S4: Schematic representation of  $\text{TMPS}_3$  with mixed magnetic configurations between layers and an AFM-a phase (two FM layers coupled antiferromagnetically). The ferrimagnetic configuration consists of three atoms aligned ferromagnetically per unit cell.

Configuration	BL-FePS <sub>3</sub> (ML)	BL-NiPS <sub>3</sub> (ML)
	$\Delta E$ (meV)	$\Delta E$ (meV)
zigzag	0 (0)	0 (0)
Néel	3.98 (3.85)	6.07 (3.59)
zstripy	13.29 (12.098)	41.87 (30.20)
zig-Néel	0.90	3.14
zig-stripy	8.07	20.86
zig-ferri	3.59	6.04
ferri	- (5.68)	19.93 (15.13)
stripy-ferri	-	31.27
FM	20.82 (25.03)	32.73 (24.80)

Table S3: Energy difference among different magnetic configurations concerning zigzag state ( $\Delta E = E_{conf.} - E_{zigzag}$ ) in meV/M for the bilayer (BL) system with  $M_P^{S1}$  stacking. The label “-” means that the system is unstable, and the value in the parenthesis corresponds to the system in the monolayer case.

such as stripy and even ferromagnetic coupling. This observation holds beyond the bilayer, as demonstrated in the monolayer case.

## SIV.2 NiPS<sub>3</sub>: stacking magnetic configurations.

Table S4 shows the total energy for the lowest magnetic configuration for both stackings. In the case of  $M_P^{S1}$  stacking, the configurations used include zigzag-I/II, Néel, zigzag-ferri, ferri-I, and stripy-ferri-I/II. In the case of the  $M_P^{Ni}$  stacking, the configurations used are zigzag-I/II, Néel-I/II, zigzag-ferri-I, and stripy-ferri-II and AFM-a (notation I and II are the abbreviations of Conf.I and Conf. II, respectively). Fig. S4 shows a schematic representation of each configuration.

$M_P^{S1}$ -Configurations	Energy (eV)	$M_P^{Ni}$ -Configurations	Energy (eV)
zigzag-I	-112.706	zigzag-I	-110.321
zigzag-II	-112.703	zigzag-II	-110.319
Néel-I	-112.657	Néel-I	-110.278
zigzag-ferri-I	-112.624	Néel-II	-110.288
ferri-I	-112.538	zigzag-ferri-I	-110.256
stripy-ferri-II	-112.457	stripy-ferri-II	-110.129
stripy-ferri-I	-112.452	AFM-a	-110.129

Table S4: NiPS<sub>3</sub>: Total energy for  $M_P^{S1}$  and  $M_P^{Ni}$  stacking.

## SIV.3 FePS<sub>3</sub> stacking magnetic configurations:

Table S5 shows the total energy for the lowest magnetic configuration for both stackings. For  $M_P^{S1}$ , zigzag-I/II, Néel, zigzag-ferri-I, ferri-I and stripy-ferri-I. In case of  $M_P^{Ni}$ , we find zigzag-I/II, Néel-I/II, zigzag-ferri-I/II, stripy-I/II.

Table S6 shows the intralayer ( $J_1$ ,  $J_2$  and  $J_3$ ) and interlayer ( $J_4$ ,  $J_5$  and  $J_6$ ) magnetic exchange, for  $M_P^{S1}$ , by solving the eq.2 (shown in the main text) and for  $M_P^{Fe}$  solving the set of equations given by S1.

$M_P^{S^1}$ -Configurations	Energy	$M_P^{F^e}$ -Configurations	Energy
zigzag-I	-137.803	zigzag-II	-137.813
zigzag-II	-137.802	zigzag-I	-137.812
Néel-I	-137.771	Néel-I	-137.782
zigzag-Ferri-I	-137.762	Néel-II	-137.781
ferri-I	-137.703	stripy-II	-137.641
stripy-ferri-II	-137.656	stripy-II	-137.628
stripy-ferri-I	-137.622	FM	-137.745

Table S5: FePS<sub>3</sub>: Total energy for  $M_P^{S^1}$  and  $M_P^{N^i}$  stacking.

Table S6 shows the magnetic exchange for FePS<sub>3</sub> by solving Eqs. (2) and Eqs. (S1) using Table S5 values.

	Stacking	J <sub>1</sub>	J <sub>2</sub>	J <sub>3</sub>	J <sub>4</sub>	J <sub>5</sub>	J <sub>6</sub>
FePS <sub>3</sub>	$M_P^{S^1}$	1.82	0.6	-1.96	-0.06	-1.10	-0.046
	$M_P^{T^M}$	1.15	0.33	-1.29	-0.02	-0.22	-0.12

Table S6: Intralayer (J<sub>1</sub>, J<sub>2</sub>, J<sub>3</sub>) and interlayer (J<sub>4</sub>, J<sub>5</sub>, J<sub>6</sub>) exchange interaction in meV for the lowest energy stacking.

$$\begin{aligned}
E_{\text{Néel}}^{I/II} &= E_0 - \frac{NS^2}{2}((-3J_1 + 6J_2 - 3J_3) \pm \frac{1}{2}(-J_4 + 3J_5 - 6J_6)), \\
E_z^{I/II} &= E_0 - \frac{NS^2}{2}((J_1 - 2J_2 - 3J_3) \pm \frac{1}{2}(J_4 + J_5 - 2J_6)), \\
E_s^{I/II} &= E_0 - \frac{NS^2}{2}((-J_1 - 2J_2 + 3J_3) \pm \frac{1}{2}(J_4 - 3J_5 - 2J_6)), \\
E_{\text{FM}} &= E_0 - \frac{NS^2}{2}((3J_1 + 6J_2 + 3J_3) + (J_4 + 9J_5 + 6J_6)),
\end{aligned} \tag{S1}$$

#### SIV.4 Wannier orbitals: NiPS<sub>3</sub> Intralayer

Figure S5 shows the main intralayer Wannier orbitals involved for 1<sup>st</sup>, 2<sup>nd</sup>, and 3<sup>rd</sup> intralayer NN.

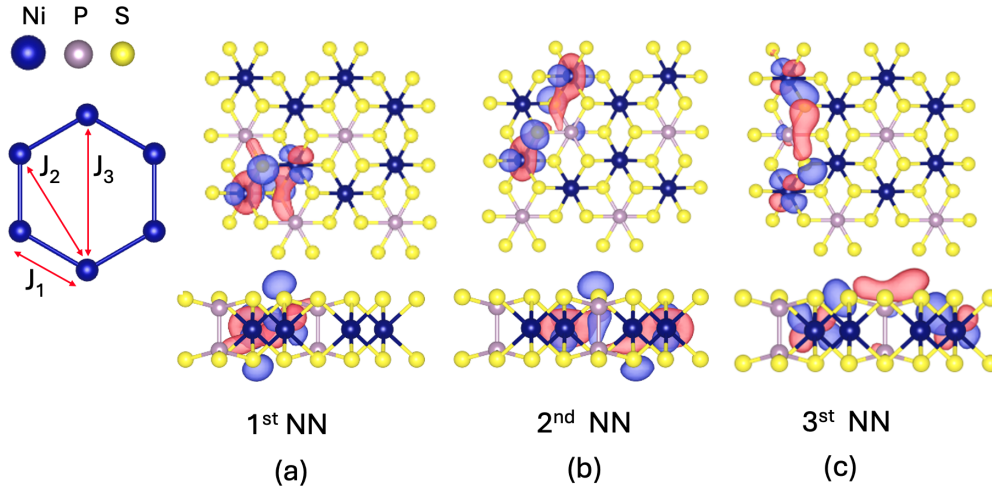


Figure S5: Localized Wannier orbitals for NiPS<sub>3</sub> intralayer nearest neighbor. (a), (b) and (c) 1<sup>st</sup>, 2<sup>nd</sup> and 3<sup>rd</sup> neighbor, respectively.